

Ionic-Like Superlattices by Charged Nanoparticles

Wenjie Wang (✉ wenjiew@ameslab.gov)

Iowa State University

Binay Nayak

Iowa State University <https://orcid.org/0000-0002-3995-4114>

Honghu Zhang

Brookhaven National Laboratory

Benjamin Ocko

Brookhaven National Laboratory

Wei Bu

Argonne National Laboratory <https://orcid.org/0000-0002-9996-3733>

Alex Travesset

<https://orcid.org/0000-0001-7030-9570>

David Vaknin

Iowa State University <https://orcid.org/0000-0002-0899-9248>

Surya Mallapragada

Iowa State University

Article

Keywords:

Posted Date: July 7th, 2023

DOI: <https://doi.org/10.21203/rs.3.rs-3112594/v1>

License:   This work is licensed under a Creative Commons Attribution 4.0 International License.

[Read Full License](#)

Additional Declarations: There is **NO** Competing Interest.

Ionic-Like Superlattices by Charged Nanoparticles

Binay P. Nayak,[†] Honghu Zhang,[‡] Wei Bu,[¶] Benjamin M. Ocko,[‡] Alex Traveset,[§]
David Vaknin,[§] Surya K. Mallapragada,^{*,†} and Wenjie Wang^{*,||}

[†]*Ames National Laboratory, and Department of Chemical and Biological Engineering, Iowa State University, Ames, Iowa 50011, United States*

[‡]*NSLS-II, Brookhaven National Laboratory, Upton, New York 11973, United States*

[¶]*NSF's ChemMatCARS, Pritzker School of Molecular Engineering, University of Chicago, Chicago, Illinois 60637, United States*

[§]*Ames National Laboratory, and Department of Physics and Astronomy, Iowa State University, Ames, Iowa 50011, United States*

^{||}*Division of Materials Sciences and Engineering, Ames National Laboratory, Ames, Iowa 50011, United States*

E-mail: suryakm@iastate.edu; wenjiew@ameslab.gov

Abstract


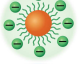
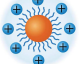

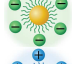
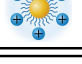
Controlling interactions among nanoparticles is paramount to achieving assemblies vital to technologies seeking to exploit their novel collective properties. Although various techniques have been advanced, robust ones are necessary for upscaling nanoparticle assembly and crystallization. Here, we show that by grafting gold nanoparticles (AuNPs) with charge-end-group-thiolated polyethylene-glycol, we control the charge of each AuNP. Such control facilitates formation of various two-dimensional structures of oppositely charged binary constituents at vapor/liquid interfaces. Using surface-sensitive synchrotron X-ray diffraction techniques, we establish the formation of distinct checker-board square lattice structures at a range of pH and molar ratios of the constituents. By regulating pH the superlattices can transform from square to the hexagonal lattice or vice versa and, to a single component superstructure at the interface. Our recipe for the control of charges and their consequent interactions among nanoparticles can be readily exploited in the assembly of devices in two and three dimensions.


Main

Recent advancements in the self-assembly of metallic nanostructures into ordered lattices have garnered significant attention by virtue of their potential applications in optoelectronics,^{1,2} plasmonics,³⁻⁵ photonics,^{6,7} catalysis,^{8,9} and energy storage devices.^{10,11} Binary nanoparticle superlattices (BNSLs), consisting of individual nanoparticles that mimic *atoms*, add a plethora of unique structures with desired properties sought for these applications.¹²⁻¹⁷ Surface grafting of nanoparticles with ligands (e.g., alkyl chains, ss-DNA, polymers, etc.) is commonly used to mediate inter-particle interactions in a suitable solvent to achieve assembly and crystallization.^{14,17-21}

Here, we explore the self-assembly of charged BNSLs at a vapor/liquid interface by grafting gold nanoparticles (AuNPs) with polyethylene glycol (PEG) terminated with either $-\text{COOH}$ or $-\text{NH}_2$ groups. In order to achieve the novel desired BNSLs, we control the charge of each nanoparticle (referred to as "super-ion") by manipulating the pH of the aqueous suspensions and mixing ratios of the constituents. In pre-

Table 1: Summary of notations for gold nanoparticles used in the manuscript with their DLS and ζ potential values. Column 2 and 3 summarizes all the symbolic and illustrative notations used for AuNPs in the manuscript. Columns 5 and 6 summarize the corresponding nanoparticles’ DLS and ζ potential values.

End group of grafted PEG	Diameter of AuNPs (nm) ¹	Symbolic notation used	Illustrative notation used	Hydrodynamic size (nm)**	ζ potential (mV)
n.a. ²	10	n.a.		17.0(2)	-40.5 ± 1.9
-COOH	10	<i>A</i>		39.5(2)	-35.7 ± 1.4
-NH ₂	10	<i>B</i>		57.7(4)*	+23.0 ± 1.9
n.a. ²	5	n.a.		10.1(23)	-30.4 ± 3.9
-COOH	5	<i>A'</i>		34.0(4)	-33.3 ± 2.1
-NH ₂	5	<i>B'</i>		40.0(4)*	+11.6 ± 1.2



¹ The diameter is from the vendor. ² The bare surface AuNPs, stabilized with citrate ligands.

* Only diffusional component of the DLS size is reported. Refer to SI for a detailed discussion.

** Only the modal size on the distribution profile is reported.

vious studies, it has been shown that BNSLs can be created by mixing charge-neutral PEG-grafted AuNPs having two different molecular weights of PEG.¹⁴ In the present study, we use AuNPs of nominal core size (5 nm and 10 nm) that both are grafted with ~ 5 kDa PEG. The rationale behind selecting AuNPs of different core sizes but with the same PEG chain length is to generate a scattering power contrast for X-ray diffraction measurements while having comparable hydrodynamic radii (Figure S1).¹⁴

We hypothesize that oppositely charged PEG grafted AuNPs, acting as super-ions, form ionic superlattices akin to ionic crystals. Unlike these ionic crystals, this approach allows for the manipulation of the relative surface charge between the two constituents. The relative charge on each particle is tuned by the manipulation of the pH of the suspension. We note that the net charge of a nanoparticle is influenced substantially by the charge of the terminal group,²² and the residual charge inherent to the AuNPs.^{23,24} Three key interactions mediate the population and crystallization at the inter-

face: the hydrophobic and Van der Waals interactions among PEG chains and the Coulombic interactions due to the charged terminals.

Here, we employ surface-sensitive synchrotron-based X-ray diffraction methods to determine the average crystal structures of BNSLs at the vapor/liquid interface, as reported in previous studies.^{14,25–27} Our findings reveal intriguing pseudo-stoichiometries and novel symmetries present for the charged BNSLs which are distinct from those observed from neutral PEG systems.^{14,27,28}

A. Charge balanced super-structures

We begin by investigating the mixtures of 1:1 molar ratios of oppositely charged particles, symbolically (*A/B'*) and (*A'/B*) (see Table 1 for nomenclatures). We note that at neutral pH, the net charge per particle differs according to the specific PEG end group; manipulating the pH controls the net charge per particle and the resultant superstructure. At neutral pH, the (*A : B'*) system does not exhibit an ac-

cumulation of particles at the interface. In contrast, the ($A' : B$) exhibits surface accumulation with the formation of a square lattice with short-range order (SRO). This finding is also based on XR analysis which shows the presence of AuNPs on the surface (see Figures S5, S6, and S8 and detailed discussion on SRO in SI). To balance the charges on the NPs, we lowered the pH values from neutral to as low as pH 2. Intriguingly, for both the $A' : B$ and $A : B'$ systems, we observe two novel structures at pH 3, as shown in Figure 1. Figure 1(a) shows a 2D diffraction pattern of the ($A' : B$) with Bragg peaks that can be indexed by a $\sqrt{2} \times \sqrt{2}$ square lattice with the unit cell edge $a \simeq 50$ nm. This notation (i.e., $\sqrt{2} \times \sqrt{2}$) is used to indicate that the structure consists of a checkerboard-like structure of oppositely charged particles and with the unit cell edge length $a \simeq \sqrt{2}a_{\text{NN}}$, where a_{NN} is the nearest neighbor (NN) distance between particles (approximately half of the average D_{H} of two individual constituents) of a PEG grafted particle. On the other hand, Figure 1(b) shows a 2D diffraction pattern for the ($A : B'$) structure with Bragg peaks that can be indexed by a $\sqrt{3} \times \sqrt{3}$ hexagonal lattice with $a \simeq 55$ nm. This notation (i.e., $\sqrt{3} \times \sqrt{3}$) is used to indicate a hexagonal lattice with unit cell edge length $a \simeq \sqrt{3}a_{\text{NN}}$ having a cell basis pseudo-formula AB'_2 . Illustrated depictions of the two observed structures and their development by variation of pH are included as insets in Figure 1 (a and b) and schematically in Figure 1 (a1 and b1) (See rationalization of the DLS of particles in SI). We note that the formation of single-orderly particles at pH 2 (depicted schematically in Figure 1(a1) and (b1)) are likely formed by the $-\text{COOH}$ grafted AuNPs (A' and A). This can be rationalized by the fact that $-\text{NH}_2$ groups become more charged at pH 2, and consequently, the whole particle is sufficiently water-soluble that it does not populate the surface.

Upon lowering the pH, the $-\text{COOH}$ terminal group tends to become less negatively charged, while the $-\text{NH}_2$ terminal group becomes more positively charged. Based on the ζ -potential values from Table 1, we estimate that the effective charge ratio of A' to B is greater than

1 at neutral pH. As the pH is lowered, there is a decrease in the net charge of A' and an increase in the net charge of B . This adjustment in charge distribution leads to an effective charge ratio that approaches 1, whereupon the neutral $A'B$ checkerboard square lattice is formed. For the $A : B'$ system, in contrast to the previous scenario, the relative charge ratio of A to B' is estimated to be approximately 3 based on the ζ potential. As we decrease the pH, the effective charge distribution on these two species converges to a ratio of 2, whereupon a AB'_2 hexagonal lattice is formed.

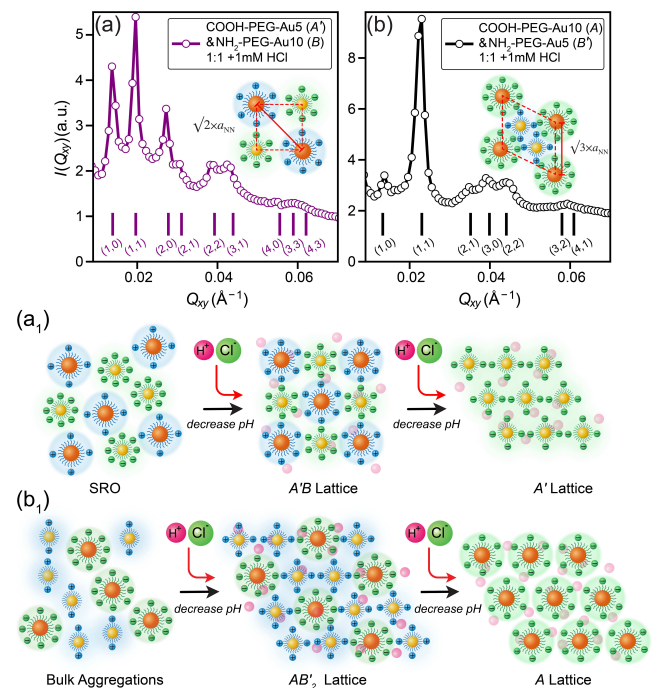


Figure 1: Formation of 2D checkerboard-like and hexagonal lattices of binary charged mixtures tuned by the effective surface-charge density. GISAXS line-cut profiles of an equimolar mixture of (a) A' & B (b) A & B' at 1mM HCl. Vertical bars represent the calculated peak positions for the corresponding lattices with their respective Miller indices mentioned below them. Insets depict ideal lattices (Refer to Table 1 for key notations). (a1) and (b1) shows the schematic illustration of lattice transitions with the addition of HCl. At a given pH (pH=3), the mixture of A' & B forms a $\sqrt{2} \times \sqrt{2}$ square lattice structure. By interchanging the core diameters of AuNP, the system changes from a square lattice to a $\sqrt{3} \times \sqrt{3}$ hexagonal lattice due to the differences in total surface charge which is dominated by the surface area of each particle. On further increasing the pH (pH=2), the surface is occupied with the $-\text{COOH}$ terminated particles due to an increase in solubility of $-\text{NH}_2$ terminated particles.

To corroborate and complement the nominal structures deduced from the GISAXS, XR experiments on the same samples under the exact conditions have been performed. Analysis of the XR provides the characteristic thickness of

the film and surface density of AuNPs. Figure S8 in the SI shows normalized XR scans and the corresponding extracted electron density (ED) profiles. The bell-shaped peak in the ED profiles represents the excess ED due to the AuNPs film confirming a single layer of the constituents AuNPs, i.e., 5 and 10 nm. As shown in the SI Table S2, the surface densities of AuNPs are consistent with the GISAXS analysis above. This shows that the X-ray reflectivity properly estimates the pseudo-stoichiometry of the ionic-like crystals at the interface. The experiments displayed in Figure 1 demonstrate control over the total charge of the constituents through manipulation of the pH and core size (dominated by the total number of end groups). Below, we show that the same and other superstructures can be formed by manipulation of the mixing ratio of the various constituents.

B. Bulk mixing-ratios induced superstructures

As previously demonstrated above, the formation of a more exotic structure is observed at a pH level of 3. Consequently, we delve into a more comprehensive exploration of the influence exerted by the bulk mixing ratios at this specific pH level. Figure 2 shows the GISAXS profiles of $A : B$ and $A : B'$ systems at different molar mixing ratios for a fixed pH of 3. Figure 2 (a), diffraction pattern from a 2:1 molar mixing ratio of $A' : B$ that is consistent with the formation of a $\sqrt{3} \times \sqrt{3}$ hexagonal structure. The unit cell of this structure is similar to the one depicted in Figure 1 (b), but with a pseudo-stoichiometric formula of A'_2B in contrast to AB'_2 . We note that the lattice constant for the AB'_2 structure in Figure 1 (b) $a \simeq 55$ nm, but for A'_2B in Figure 2 (a) $a \simeq 49$ nm is consistent with the Coulombic repulsion between the B' particles, since at the specified pH, the two B' particles within the AB'_2 unit cell maintain a high charge. This leads them to repel each other, causing the formation of a unit cell marginally larger than what is observed for the A'_2B unit cell. This disparity can be linked to the two A' particles, which display an almost neutral charge state. This A'_2B structure is also

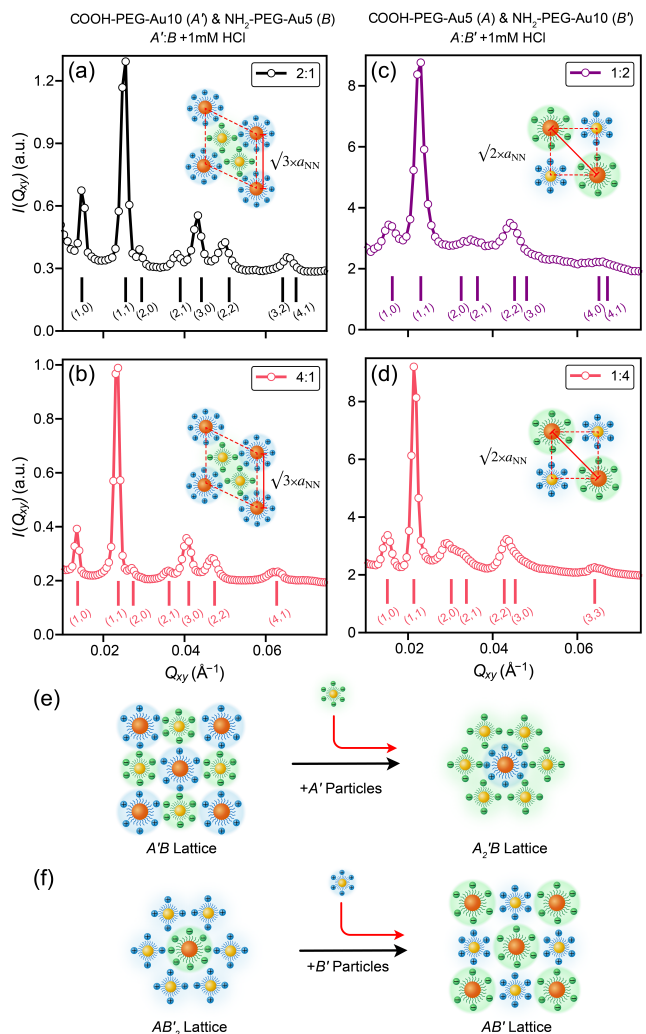


Figure 2: Mixing-ratio-induced lattice transitions from a $A'B$ square lattice to A'_2B hexagonal lattice and from a AB'_2 hexagonal lattice to AB' hexagonal lattice. GISAXS line-cut profiles and schematic lattice representations of binary mixtures of A' and B at (a) 2:1 (b) 4:1 molar ratios, and binary mixtures of A and B' at (c) 1:2 (d) 1:4 molar ratios, at 1mM HCl as indicated. Insets depict ideal lattices (Refer to Table 1 for key notations). Vertical bars represent the calculated peak positions for the corresponding lattices with their respective Miller indices mentioned below them. (e) and (f) represents a schematic illustration of lattice transitions. At a given pH ($\text{pH}=3$), the equimolar mixture of $A' : B$ forms a 2D $\sqrt{2} \times \sqrt{2}$ $A'B$ square lattice (Figure 1 (a)). On further increasing the molar ratio to 2:1, the lattice transforms to a $\sqrt{3} \times \sqrt{3}$ A'_2B hexagonal lattice, which remains unchanged at a 4:1 molar ratio, indicating the structural resistance to increasing ratios. Similarly, the equimolar mixture of $A : B'$ forms a 2D $\sqrt{3} \times \sqrt{3}$ AB'_2 hexagonal lattice (Figure 1 (b)). By further increasing the molar ratio to 1:2, the lattice transforms to a $\sqrt{2} \times \sqrt{2}$ AB' square lattice, which remains unchanged at a 4:1. These results emphasize the tunability of lattice structures in binary mixtures, showcasing their structural robustness.

corroborated by XR analysis as discussed in reference to Figure 1 (a) and in the SI. As noted above, a 1:1 mixing ratio of the same $A' : B$ constituents, leads to the formation of a $\sqrt{2} \times \sqrt{2}$ square lattice. As the molar ratio is increased (by increasing the amount of A' constituent),

the system undergoes a transition from a square lattice to a hexagonal lattice, and this hexagonal lattice remains robust as the molar ratio is further increased to 4:1. Similarly, Figure 2 (c) shows the formation of a $\sqrt{2} \times \sqrt{2}$ square-lattice originating from the 1:2 mixture of $A : B'$ constituents. The unit cell of this structure is similar to the one mentioned in Figure 1 (a) but has a pseudo-stoichiometric formula of AB' due to its individual constituents. Figure 2 (d) shows the formation of a similar AB' square lattice with an increase in the molar mixing ratio to 1:4 from 1:2, indicating the robustness of the square lattice with the increase in mixing ratios. Unlike the earlier case of the $A' : B$ system, in the $A : B'$ system, the transition from a 1:1 ratio leads to a change from a $\sqrt{3} \times \sqrt{3}$ hexagonal lattice to a $\sqrt{2} \times \sqrt{2}$ square lattice.

A central conclusion from the present and previous sections is that the surface charge density created by the $-\text{COOH}$ group is larger than the $-\text{NH}_2$ terminal group, consistent with ζ potential values and published results.²² Also, the total charge on each particle scales with the surface area of the core. These differences can be taken advantage of by manipulating the pH in the suspension to vary the net surface charge. Next, we present the effect of varying the pH on the crystallization of the same system with fixed molar mixing ratios.

C. pH-controlled super-structures

Figure 3 shows GISAXS measurements of $A' : B$ at a 2:1 molar ratio at four different pH values. At neutral pH, the system spontaneously forms a checkerboard crystal structure with a relatively large lattice constant of $a \simeq 51$ nm and is depicted schematically in the inset. Such a large lattice constant is unusual for a long-range order (LRO) of a neutral 5KDa PEG/AuNP system.¹⁴ To rationalize this, we note that previous results indicate that $-\text{NH}_2$ (B particles) terminated particles spontaneously populate the surface due to a lower positive surface charge, while the $-\text{COOH}$ (A' particles) terminated particles carry a higher total negative charge density.²² This results in a repulsion between the A' particles, leading to

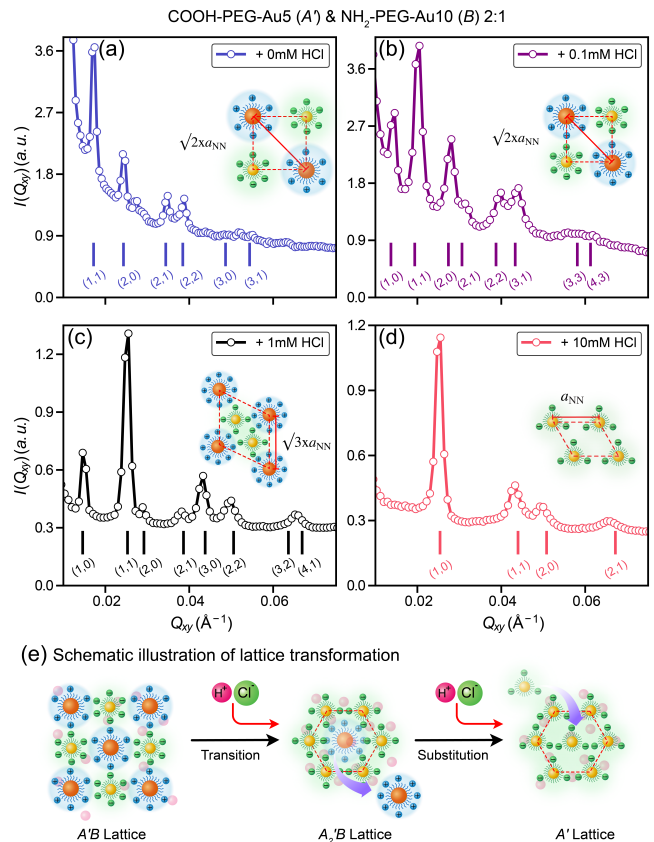


Figure 3: pH-induced symmetry transition in 2:1 mixture of COOH-PEG-Au5 & NH₂-PEG-Au10. GISAXS line-cut profiles and schematic lattice representations of a binary mixture of A' & B at a 1:2 molar ratio, at (a) 0mM (b) 0.1mM (c) 1mM (d) 10mM HCl molar concentration. Insets depict ideal lattices (Refer to Table 1 for key notations). Vertical bars represent the calculated peak positions for the corresponding lattices with their respective Miller indices mentioned below them. The mixture forms a 2D $\sqrt{2} \times \sqrt{2}$ square lattice at $[\text{HCl}] = 0.1$ mM, transforms to a $\sqrt{3} \times \sqrt{3}$ hexagonal lattice at $[\text{HCl}] = 1$ mM, and further to a 1×1 hexagonal lattice at $[\text{HCl}] = 10$ mM, indicating the pH sensitivity of the lattice formed. (e) Represents a schematic illustration of lattice transformation from a $\sqrt{2} \times \sqrt{2}$ square lattice to a $\sqrt{3} \times \sqrt{3}$ hexagonal lattice and further to a 1×1 hexagonal lattice.

the increased unit cell size, as depicted schematically by a halo of the A' particles with an enlarged effective cross-section. To counteract this effect, we add HCl to the system, which balances the net charge on A' and B particles, and as a result, the lattice constant is reduced by $\sim 20\%$ to $a \simeq 43$ nm as deduced from the diffraction patterns in Figure 3 (a) and (b). Consistently, decreasing the pH increases the propensity of A' particles to populate the surface as the B particles became more soluble due to an increase in positive charge density. Here we note that the relative enrichment of A' particles at the interface, compelling the system to settle into a pseudo-stoichiometric A'_2B

hexagonal unit cell as extracted from Figure 3(c) and shown schematically in the inset. This formulation suggests an occupation of two relative surface-rich A' particles in coordination with each B particle. To validate the proposed pseudo-stoichiometry of the emergent nominal structures, we conducted a meticulous XR analysis on the aforementioned samples. The findings from this analysis are encapsulated in Figure S12. A summary of the average surface coverage, as inferred from XR with that derived from GISAXS, is presented in Figure S12 and Table S2. Remarkably, at pH=3, the computed surface coverage of the A'_2B structure aligns perfectly with the coverage inferred from XR profiles. This concurrence unequivocally corroborates our proposed pseudo-stoichiometry A'_2B , thereby underscoring its relevance and validity in this system. This trend of lowering the charge on the $-\text{COOH}$ group of A' particles, continues by lowering the pH and finally leading to a simple hexagonal structure consisting of the A' particles as shown in the diffraction pattern and depicted in Figure 3(d).²² We rationalize that the surface predominance of particles A' can be attributed to the enriched charge density of particle B , which potentially augments the solubility of particles B , thereby encouraging their bulk presence. To summarize, the effect of lowering the pH, and the progression of structural transitions are illustrated in Figure 3(e) conceptually.

Conclusions

In this study, we control the total surface charge of PEG-grafted AuNPs by adding carboxylic or amine terminal groups and by varying the pH. Based on previous results and ζ -potential measurements, we expect the carboxylic acid group to be negatively charged, while the amine group to be positively charged. Previous experiments have shown that under neutral pH conditions, $-\text{COOH}$ seems to be totally charged by dissociating into $-\text{COO}^-$, resulting in the grafted AuNPs in neutral pH fully dispersed in the suspension. By contrast, the $-\text{NH}_2$ is partially charged by protonation, which makes them

migrate to the vapor/liquid interface spontaneously at neutral pH. Therefore, in order to take advantage of ordering by Coulombic interactions, we modified the pH of the suspension and control the charges of both end groups. In general, our results show that lowering the pH reduces the charge in the $-\text{COOH}$ group and increases the charge in the $-\text{NH}_2$ group. Our Zeta potential measurements confirm this finding and provide a quick path for predicting the possible structures of such BNSLs. Using surface-sensitive X-ray diffraction techniques (GISAXS, XR) we test the above hypotheses and determine the actual structures of AuNPs under various conditions. The main results of our study are summarized in a pH-mixing-ratios phase diagram in Figure 4 and as follows: (1) A checker-board square lattice can be achieved by either lowering the pH and/or manipulating molar mixing ratios. (2) By further lowering the pH or increasing the molar ratio, the system transforms from a checkerboard structure to a hexagonal structure with a pseudo-stoichiometry of $A'B$, and AB' to, A'_2B and AB'_2 . This tunability enables the tailoring of material properties by manipulating the molar ratios of the constituents. (3) In the extreme case of low pH, one of the constituents (likely $-\text{COOH}$ terminated PEG-AuNP) forms a single-particle hexagonal structure akin to neutral PEG-grafted AuNPs structures at the vapor/liquid interface.

Methods

Materials Preparations

Unconjugated citrate-capped bare AuNPs (nominal core diameter 5 and 10 nm) were purchased from Ted Pella Inc., and their size distributions were independently validated by small-angle X-ray scattering.^{14,26} PEG of average molecular weight 5 kDa, with one end terminated with thiol (HS) and the other with either carboxyl ($-\text{NH}_2$) or amine($-\text{COOH}$), were purchased from Creative PEGworks (NC, USA). AuNPs were functionalized with HS-PEG-COOH or HS-PEG-NH₂ by the ligand

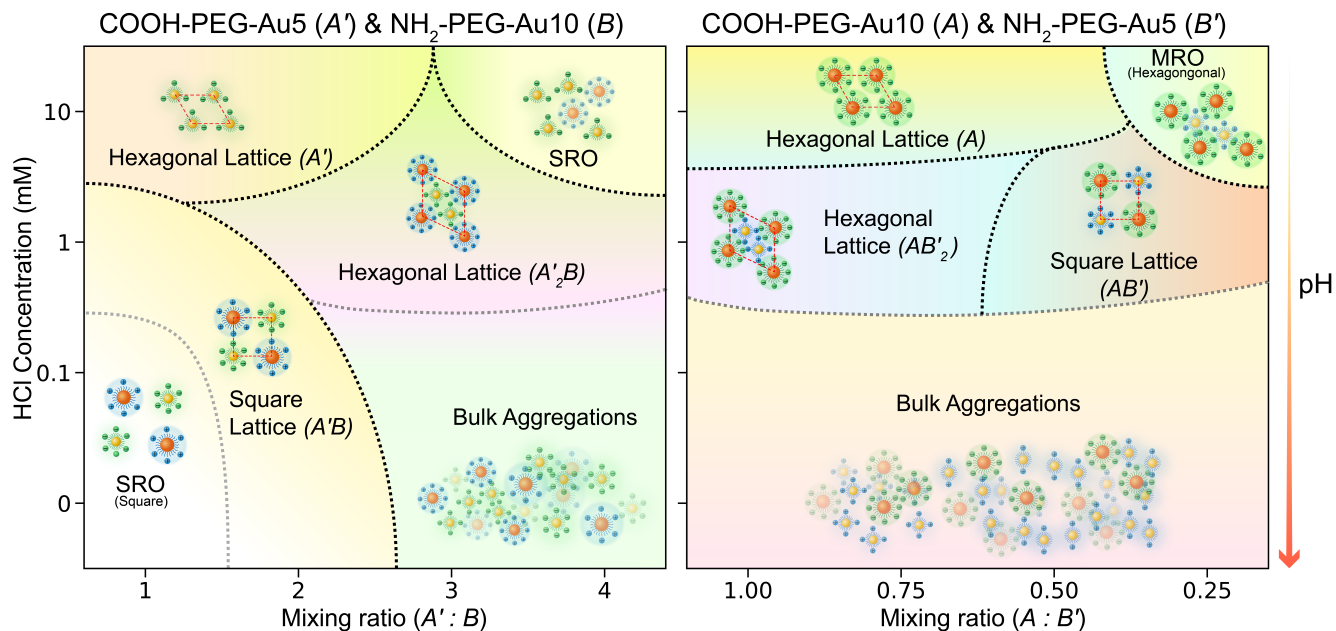


Figure 4: Schematic phase diagram of all structures reported in Table 2. Left figure shows a schematic phase diagram of a binary mixture of A' and B , and the right figure shows a schematic phase diagram of a binary mixture of A and B' as a function of molar mixing ratio and HCl concentration. The axes are not to be scaled, and the phase boundaries are hypothetical.

exchange method as described below.^{14,28} PEG ligands are first dissolved in 1 M sodium chloride (NaCl) solution and mixed thoroughly. The PEG-NaCl solution in excess is mixed with a certain amount of AuNP suspensions and incubated for at least 24 hours with continuous mixing with a Roto-Shake Genie (Scientific Industries, NY, USA).¹⁴ The unbound PEG from the resulting PEG-grafted AuNPs was removed by centrifugation thrice at 21000 RCF for 90 minutes. In this study, the term PEG-AuNP represents PEG-grafted AuNPs in general, while x -PEG-AuNP y indicates AuNPs of y core diameter (i.e., $y = 10$ and 5 nm) terminated with x group (i.e., $x =$ either $-\text{COOH}$, or $-\text{NH}_2$ groups) of PEG. For instance, COOH-PEG-AuNP10 refers to gold nanoparticles of an average diameter of 10 nm, functionalized with carboxyl-terminated PEG. For convenience, we represent each grafted nanoparticle as shown by letters and symbols in Table 1. The final concentration of the PEG-AuNPs was determined by measuring their absorbance using ultraviolet-visible (UV-vis) spectroscopy (NanoDrop One Microvolume instrument from Thermo Fischer Scientific) and then adjusted to ~ 15 nM and ~ 60 nM for 10 and 5 nm nanoparticles, respectively. Subsequently, the

hydrodynamic diameter (D_H) of the grafted nanoparticles was determined using dynamic light scattering (DLS) with a NanoZS90 and its associated software Zetasizer (Malvern, United Kingdom). To quantify the surface charge of the PEG-grafted AuNPs, zeta potential measurements were conducted using the NanoZS90 instrument. The results of these measurements are listed in Table 1. The COOH-PEG-AuNPs and NH_2 -PEG-AuNPs were characterized by opposite electrical charge and enlarged hydrodynamic size, indicating the successful grafting of PEG with distinct terminal groups. More detailed information on PEG grafting and characterization is provided in the SI.

For the liquid surface X-ray diffraction experiments, the nanoparticle suspensions were mixed for desired molar ratio and incubated for approximately 15 minutes before loading onto a stainless steel trough. The trough with the sample was contained in an enclosed sample chamber purged with water-saturated helium on the x-ray liquid surface spectrometer.²⁹ Calculated amount of stock HCl solution was added incrementally to the same mixture suspension for a sequence of target pH values and incubated for about 20 minutes before X-ray measurements.

Table 2: Summary of GISAXS analysis based on data collected at APS and NSLS-II for the binary mixture of charged AuNPs. GISAXS suggests long-range order (LRO) for most of the structures, while short-range order (SRO) and meso-range order (MRO) are observed in a few cases. Refer to the SI for more details.

AuNP size (nm)		Mixing ratio	[HCl] (mM)	Lattice type (Stoichiometry)		Unit cell edge length* a (nm)
COOH-PEG	NH ₂ -PEG					
A'	B	$A' : B$				
5	10	1:1	0	$\sqrt{2} \times \sqrt{2}$	Square ($A'B$)	49.6 ± 2.3
			0.1	$\sqrt{2} \times \sqrt{2}$	Square ($A'B$)	47.3 ± 2.1
			1	$\sqrt{2} \times \sqrt{2}$	Square ($A'B$)	45.3 ± 2.0
			10	1×1	Hexagonal (likely A')	31.5 ± 1.2
5	10	2:1	0	$\sqrt{2} \times \sqrt{2}$	Square ($A'B$)	50.9 ± 2.5
			0.1	$\sqrt{2} \times \sqrt{2}$	Square ($A'B$)	43.3 ± 1.8
			1	$\sqrt{3} \times \sqrt{3}$	Hexagonal (A'_2B)	49.3 ± 1.6
			10	1×1	Hexagonal (likely A')	28.5 ± 1.0
5	10	4:1	0	-		-
			0.1	-		-
			1	$\sqrt{3} \times \sqrt{3}$	Hexagonal (A'_2B)	53.2 ± 1.9
			10	-	SRO	-
A	B'	$A : B'$				
10	5	1:1	0	-		-
			0.1	-		-
			1	$\sqrt{3} \times \sqrt{3}$	Hexagonal (AB'_2)	54.6 ± 2.0
			10	1×1	Hexagonal (likely A)	30.5 ± 1.1
10	5	1:2	0	-		-
			0.1	-		-
			1	$\sqrt{2} \times \sqrt{2}$	Square (AB')	38.6 ± 1.4
			10	1×1	Hexagonal (likely A)	29.3 ± 1.0
10	5	1:4	0	-		-
			0.1	-		-
			1	$\sqrt{2} \times \sqrt{2}$	Square (AB')	41.6 ± 1.7
			10	$\sqrt{3} \times \sqrt{3}$	MRO Hexagonal (Uncertain)	54.7 ± 2.0

* For 2D 1×1 hexagonal structure, lattice constant, $a = 4\pi/(\sqrt{3}Q_{10})$, for 2D $\sqrt{3} \times \sqrt{3}$ hexagonal structure, lattice constant, $a = 4\pi/(Q_{11})$ and for 2D square structure, lattice constant, $a = 2\sqrt{2}\pi/Q_{11}$. The error-bar estimation is described in the supplementary section.

X-ray Diffraction Measurements

Synchrotron-based *in-situ* liquid surface X-ray scattering experiments were performed at NSF's ChemMatCARS Sector 15, Advanced Photon Source, Argonne National Laboratory, and at SMI beamline open platform liquid surfaces (OPLS) end station, National Synchrotron Light Source II (NSLS-II),

Brookhaven National Laboratory with an incident X-ray energy 10 and 9.7 keV, respectively. Liquid-surface specular X-ray reflectivity (XR) and grazing incidence small-angle X-ray scattering (GISAXS) were conducted to determine the density profile across the vapor/liquid interface and the in-plane arrangement of nanoparticle assembly at the aqueous surface. The experimental instrumental setup and measurement

protocols at these two beamlines are detailed in previous reports.^{5,14,28}

Below is a brief description of data collection and presentation. Incident X-rays of wavevector \vec{k}_i are incident upon the aqueous surface at grazing angles, and scattered X-rays of wavevector \vec{k}_f are recorded using an area detector, where the scattering intensity is recorded as a function of the scattering vector \vec{Q} , $\vec{Q} = \vec{k}_f - \vec{k}_i$. Q_z and Q_{xy} denote the vertical and horizontal components of \vec{Q} , respectively. For XR, the reflectivity $R(Q_z)$ is normalized to the Fresnel reflectivity R_F calculated for the corresponding ideal flat surface solutions. The electron density (ED) profiles along the vertical direction z , $\rho(z)$, are obtained using Paratt’s recursive method from fitted R/R_F data.³⁰ The scattered intensities in GISAXS are presented as 2D images in terms of Q_{xy} and Q_z . A line-cut intensity profile of GISAXS, as a function of Q_{xy} is integrated over Q_z range 0.01–0.03 \AA^{-1} (see Figure S2), denoted as $I(Q_{xy})$. The diffraction peaks are marked with Miller indices (h, k) for the identified 2D lattice type.

Supporting Information

The Supporting Information is available free of charge on the Nature Publications website at DOI: xxxxx/yyyyy

Data Availability

The findings of this study are supported by data found within the article and the provided Supplementary Information. Further relevant information and source data can be obtained from the corresponding author upon making a reasonable request.

Acknowledgements

The authors would like to thank Hyeong Jin Kim for initiating this work at Ames National Laboratory. Research was supported by the U.S. Department of Energy (U.S. DOE), Office of Basic Energy Sciences, Division of Ma-

terials Sciences and Engineering. Iowa State University operates Ames National Laboratory for the U.S. DOE under Contract DE-AC02-07CH11358. Part of this research used the Open Platform Liquid Surfaces (OPLS) end station of the Soft Matter Interfaces Beamline (SMI, Beamline 12-ID) at the National Synchrotron Light Source II, a U.S. Department of Energy (DOE) Office of Science User Facility operated for the DOE Office of Science by Brookhaven National Laboratory under Contract No. DE-SC0012704. Part of this research used NSF’s ChemMatCARS Sector 15. NSF’s ChemMatCARS Sector 15 is supported by the Divisions of Chemistry (CHE) and Materials Research (DMR), National Science Foundation, under grant number NSF/CHE-1834750. The use of the Advanced Photon Source, an Office of Science User Facility operated for the U.S. Department of Energy (DOE) Office of Science by Argonne National Laboratory, was supported by the U.S. DOE under Contract No. DE-AC02-06CH11357.

Author contributions

WW, DV, and SM conceived and supervised the project. BN, DV, and WW designed, conducted the experiments, and analyzed the data. BN, WW, and DV wrote the manuscript. BMO, WB, and HZ supported in the X-ray scattering experiments, data acquisition, and data processing. AT provided theoretical input. SM, DV, and WW secured the funding for the project. All co-authors read and reviewed the manuscript.

References

1. Talapin, D. V.; Lee, J.-S.; Kovalenko, M. V.; Shevchenko, E. V. Prospects of colloidal nanocrystals for electronic and optoelectronic applications. *Chemical reviews* **2010**, *110*, 389–458.
2. Sung, J.; Jo, P. S.; Shin, H.; Huh, J.; Min, B. G.; Kim, D. H.; Park, C. Transparent, Low-Electric-Resistance Nanocompos-

- ites of Self-Assembled Block Copolymers and SWNTs. *Advanced Materials* **2008**, *20*, 1505–1510.
3. Fan, J. A.; Wu, C.; Bao, K.; Bao, J.; Bardhan, R.; Halas, N. J.; Manoharan, V. N.; Nordlander, P.; Shvets, G.; Capasso, F. Self-assembled plasmonic nanoparticle clusters. *science* **2010**, *328*, 1135–1138.
 4. Tao, A.; Sinsersuksakul, P.; Yang, P. Tunable plasmonic lattices of silver nanocrystals. *Nature nanotechnology* **2007**, *2*, 435–440.
 5. Kim, H. J.; Wang, W.; Bu, W.; Mallapragada, S.; Vaknin, D. Lamellar and Hexagonal Assemblies of PEG-Grafted Silver Nanoparticles: Implications for Plasmonics and Photonics. **2022**,
 6. Yadav, A.; Gerislioglu, B.; Ahmadi-vand, A.; Kaushik, A.; Cheng, G. J.; Ouyang, Z.; Wang, Q.; Yadav, V. S.; Mishra, Y. K.; Wu, Y., *et al.* Controlled self-assembly of plasmon-based photonic nanocrystals for high performance photonic technologies. *Nano Today* **2021**, *37*, 101072.
 7. Yazdani, N.; Jansen, M.; Bozyigit, D.; Lin, W. M.; Volk, S.; Yarema, O.; Yarema, M.; Juranyi, F.; Huber, S. D.; Wood, V. Nanocrystal superlattices as phonon-engineered solids and acoustic metamaterials. *Nature Communications* **2019**, *10*, 4236.
 8. Yu, C.; Guo, X.; Muzzio, M.; Seto, C. T.; Sun, S. Self-Assembly of Nanoparticles into Two-Dimensional Arrays for Catalytic Applications. *ChemPhysChem* **2019**, *20*, 23–30.
 9. Gajraj, V.; Devi, P.; Kumar, R.; Sundriyal, N.; Reddy, M.; Mariappan, C. Self-assembly of novel cobalt iron phosphate nanoparticles for the solid-state supercapattery and high-performance hydrogen evolution reaction. *International Journal of Hydrogen Energy* **2023**,
 10. Wang, D.; Kou, R.; Choi, D.; Yang, Z.; Nie, Z.; Li, J.; Saraf, L. V.; Hu, D.; Zhang, J.; Graff, G. L., *et al.* Ternary self-assembly of ordered metal oxide- graphene nanocomposites for electrochemical energy storage. *ACS nano* **2010**, *4*, 1587–1595.
 11. Pomerantseva, E.; Bonaccorso, F.; Feng, X.; Cui, Y.; Gogotsi, Y. Energy storage: The future enabled by nanomaterials. *Science* **2019**, *366*, eaan8285.
 12. Urban, J. J.; Talapin, D. V.; Shevchenko, E. V.; Kagan, C. R.; Murray, C. B. Synergism in binary nanocrystal superlattices leads to enhanced p-type conductivity in self-assembled PbTe/Ag₂Te thin films. *Nature materials* **2007**, *6*, 115–121.
 13. Dong, A.; Chen, J.; Vora, P. M.; Kikkawa, J. M.; Murray, C. B. Binary nanocrystal superlattice membranes self-assembled at the liquid–air interface. *Nature* **2010**, *466*, 474–477.
 14. Kim, H. J.; Wang, W.; Zhang, H.; Freychet, G.; Ocko, B. M.; Travesset, A.; Mallapragada, S. K.; Vaknin, D. Binary superlattices of gold nanoparticles in two dimensions. *The Journal of Physical Chemistry Letters* **2022**, *13*, 3424–3430.
 15. Deng, K.; Xu, L.; Guo, X.; Wu, X.; Liu, Y.; Zhu, Z.; Li, Q.; Zhan, Q.; Li, C.; Quan, Z. Binary nanoparticle superlattices for plasmonically modulating upconversion luminescence. *Small* **2020**, *16*, 2002066.
 16. Ye, X.; Chen, J.; Diroll, B. T.; Murray, C. B. Tunable plasmonic coupling in self-assembled binary nanocrystal superlattices studied by correlated optical microspectrophotometry and electron microscopy. *Nano letters* **2013**, *13*, 1291–1297.
 17. Shevchenko, E. V.; Talapin, D. V.; O’Brien, S.; Murray, C. B. Polymorphism in AB₁₃ nanoparticle superlattices: an example of semiconductor- metal metamaterials.

- Journal of the American Chemical Society* **2005**, *127*, 8741–8747.
18. Macfarlane, R. J.; Lee, B.; Jones, M. R.; Harris, N.; Schatz, G. C.; Mirkin, C. A. Nanoparticle superlattice engineering with DNA. *science* **2011**, *334*, 204–208.
 19. Kalsin, A. M.; Fialkowski, M.; Paszewski, M.; Smoukov, S. K.; Bishop, K. J.; Grzybowski, B. A. Electrostatic self-assembly of binary nanoparticle crystals with a diamond-like lattice. *science* **2006**, *312*, 420–424.
 20. Wang, K.; Li, F.; Jin, S.-M.; Wang, K.; Tian, D.; Hussain, M.; Xu, J.; Zhang, L.; Liao, Y.; Lee, E., *et al.* Chain-length effect on binary superlattices of polymer-tethered nanoparticles. *Materials Chemistry Frontiers* **2020**, *4*, 2089–2095.
 21. Kostianen, M. A.; Hiekkataipale, P.; Laiho, A.; Lemieux, V.; Seitsonen, J.; Ruokolainen, J.; Ceci, P. Electrostatic assembly of binary nanoparticle superlattices using protein cages. *Nature nanotechnology* **2013**, *8*, 52–56.
 22. Kim, H. J.; Nayak, B. P.; Zhang, H.; Ocko, B. M.; Travesset, A.; Vaknin, D.; Mallapragada, S. K.; Wang, W. Two-dimensional assembly of nanoparticles grafted with charged-end-group polymers. *arXiv preprint arXiv:2305.16512* **2023**,
 23. Doane, T. L.; Cheng, Y.; Babar, A.; Hill, R. J.; Burda, C. Electrophoretic Mobilities of PEGylated Gold NPs. *Journal of the American Chemical Society* **2010**, *132*, 15624–15631.
 24. Wang, W.; Zhang, H.; Kuzmenko, I.; Mallapragada, S.; Vaknin, D. Assembling bare Au nanoparticles at positively charged templates. *Scientific reports* **2016**, *6*, 1–9.
 25. Zhang, H.; Nayak, S.; Wang, W.; Mallapragada, S.; Vaknin, D. Interfacial self-assembly of polyelectrolyte-capped gold nanoparticles. *Langmuir* **2017**, *33*, 12227–12234.
 26. Zhang, H.; Wang, W.; Akinc, M.; Mallapragada, S.; Travesset, A.; Vaknin, D. Assembling and ordering polymer-grafted nanoparticles in three dimensions. *Nanoscale* **2017**, *9*, 8710–8715.
 27. Kim, H. J.; Hossen, M. M.; Hillier, A. C.; Vaknin, D.; Mallapragada, S. K.; Wang, W. Interfacial and bulk assembly of anisotropic gold nanostructures: implications for photonics and plasmonics. *ACS Applied Nano Materials* **2020**, *3*, 8216–8223.
 28. Zhang, H.; Wang, W.; Mallapragada, S.; Travesset, A.; Vaknin, D. Macroscopic and Tunable Nanoparticle Superlattices. *Nanoscale* **2017**, *9*, 164–171.
 29. Pershan, P. S.; Schlossman, M. *Liquid Surfaces and Interfaces: Synchrotron X-ray Methods*. **2012**,
 30. Als-Nielsen, J.; Desmond, M. *Elements of Modern X-ray Physics*, 2nd ed.; Wiley, 2011.
 31. Kim, H. J.; Wang, W.; Zhang, H.; Freychet, G.; Ocko, B. M.; Travesset, A.; Mallapragada, S. K.; Vaknin, D. Effect of polymer chain length on the superlattice assembly of functionalized gold nanoparticles. *Langmuir* **2021**, *37*, 10143–10149.

Cover Figure (Table of content)

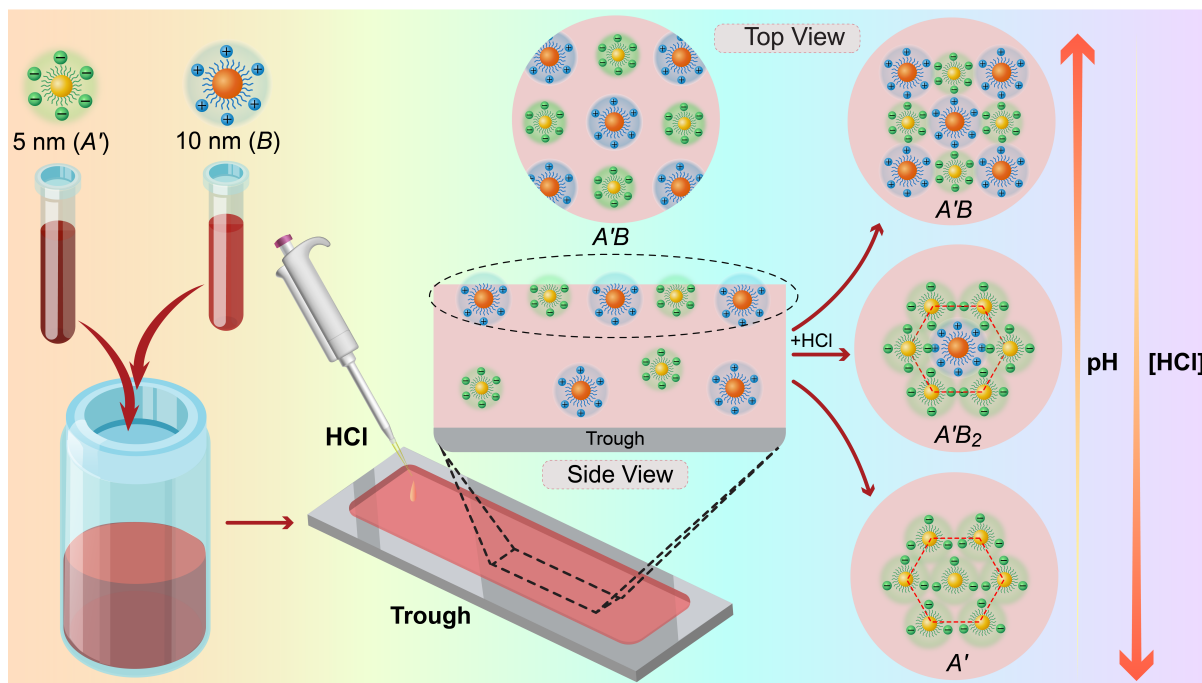


Figure 5: Schematic illustration of lattice transition and experimental procedure The two vials contain suspensions of AuNPs that are grafted with thiolated PEG and terminating with either -NH_2 or -COOH . The core (5 or 10 nm) is chosen to enhance the scattering contrast between the two constituents. The two constituents are mixed with desired molar mixing ratio into a secondary vial and spread into a stainless-steel trough. Surface-sensitive X-ray scattering, including X-ray reflectivity and grazing incidence small-angle X-ray scattering, is conducted on the filled-trough surface. By adjusting the pH and molar-mixing ratio, we obtained various structures, including checker-board-like structures and binary hexagonal structures, summarized in Figure 4.

Supplementary Files

This is a list of supplementary files associated with this preprint. Click to download.

- [IonicLikeSuperlatticesAssembliesbyChargedNanoparticlesSI.pdf](#)